An Automated Technique for Carotid Far Wall Classification using Grayscale Features and Wall Variability

Abstract

Purpose. This paper describes a Computer Aided Diagnostic (CAD) method for identification of symptomatic and asymptomatic carotid ultrasound images to be applied for the early diagnosis of atherosclerosis, on images that could contain a light plaque.

Methods. The proposed system (called Atheromatic™) automatically computes the Intima Media Thickness (*IMT*) far wall region from the input image using AtheroEdge™, calculates nonlinear features based on Higher Order Spectra (HOS), and uses these features and *IMT* and *IMT* wall variability ($IMTV_{poly}$). Each image is associated to a feature vector that is then labeled as symptomatic or asymptomatic (*Sym*/*Asym*) by using a multi-classifiers system.

Results. We used a database of 118 patients and the highest accuracy of 99.1% was registered by the Support Vector Machine classifier using seven features. These features, relevant to discriminate *Sym/Asym*, included *IMT* and $IMTV_{poly}$, along with the bispectral entropies of the distal wall image at the angles of 77°, 78°, and 79°.

Conclusions. Classification in *Sym/Asym* of the distal carotid wall is feasible and accurate and it could be useful to the early detection of atherosclerosis and to identify the patients with potential higher cardiovascular risk.

Keywords—Atherosclerosis, classification, automatic wall segmentation, intima-media thickness variability, ultrasounds.

I. INTRODUCTION

Carotid atherosclerosis is an inflammatory progressive disease in which stenosis occurs due to the formation of plaques [1]. Pieces of plaque can result in embolization, which can lead to heart attack and stroke [2]. Recent global statistics from the World Health Organization (WHO) estimates that by 2030, about 23.6 million people may die due to cardiac diseases like heart disease and stroke [3]. Generally, the patients are chosen for surgery based on symptoms and degree of stenosis. However, low stenotic plaques may cause symptoms [4] and highly stenotic plaques may be asymptomatic [5]. Hence, in order to assist the vascular surgeons to decide the accurate treatment, it is necessary to differentiate symptomatic (*Sym*) and asymptomatic (*Asym*) classes correctly.

The assessment of *Sym/Asym* patients is eased by the use of Computer Aided Diagnostic (CAD) tools. Most of the CAD studies[6-8] have proposed classification techniques that use grayscale features from plaque regions. This is because the composition of plaques from *Sym* patients is significantly different from that from *Asym* patients [9]. Our objective, in this work, was to develop an early tissue classification technique that characterizes the early changes in the Far Wall Region (FWR) of the CCA in order to differentiate *Sym* vs. *Asym* groups before the wall plaque onset, because studies have shown that progressive atherosclerotic lesion starts with the intimal wall region thickening[10]. We have used the variability of the carotid intima-media thickness (*IMT*), called the $IMTV_{poly}$, as one of the features[11,12]. Measurement of *IMT* from B-mode images manually is prone to intra and interobserver variability and time consuming. Among the CAD-based IMT measurement algorithms[13], there are several automated systems[14-17]. Since our aim was to build a fully automated system, we chose the well-validated and previously published Completely Automated Multi-resolution Edge Snapper (CAMES)[17] algorithm for

CCA FWR segmentation and subsequent LI and MA interface determination in this work. Figure 1 provides an explained echographic appearance of the B-Mode longitudinal images of a carotid artery along with the interfaces that are considered in this study.

The general framework of the proposed system (a class of Atheromatic systems) is as follows: (a) automatic segmentation of the FWR; (b) extraction of Higher Order Spectra (HOS) based features, *IMT* and $IMTV_{poly}$ from the FWR; (c) determination of ground truth of whether the segmented region belongs to *Sym* or *Asym* class based on prior presence or absence of symptoms; (d) development of classifiers using extracted features plus the ground truth labels. The following are the novel features of the proposed technique: (1) Development of an automated classification tool for the classification of automatically delineated FWR; (2) Grayscale feature extraction using non-linear HOS methods; (3) Determination and use of $IMTV_{poly}$ feature; (4) Development of an optimum classifier using a combination of HOS features, IMT and $IMTV_{poly}$; (5) Evaluation of classifier performance on FWR images.

II. MATERIALS

The study was conducted at the Department of Radiology, Azienda Ospedaliero Universitaria di Cagliari, Italy, and approval by the Institutional Review Board was obtained. We prospectively considered 59 patients (35 males, 24 females; mean age 56 years, range 37-73 years) that were examined between February 2011 and August 2011. The patients were subdivided into *Sym* and *Asym*. A subject was considered as *Sym* in the case of occurrence of transient ischemic attack (TIA) or stroke. TIA was regarded as an episode of neurological dysfunction, (hemiparesis, hemiparesthesia, dysarthria, dysphasia or monocular blindness) not exceeding 24 hours. If the episode of neurological dysfunction surpassed 24 hours it was treated as a stroke. *Sym* subjects were examined within 6 months from the TIA\Stroke event. *Asym* subjects did not show any

neurological symptom but had one of the following conditions: coronary artery disease, aortic interventions, lower leg artery surgery, or diabetes and age > 50 years. Patients with suspected embolism from a cardiac source, follow-up after intra-cerebral aneurysms, brain tumors, carotid endarterectomy, or with posterior cerebrovascular symptoms were discarded.

118 images were obtained from 37 *Sym* and 22 *Asym* consecutive in-patients. One image from left and one from right carotid were taken from each subject. In the *Sym* cases, we treated the carotid ipsilateral to the symptom as *Sym* and the one on the other side as *Asym*. Therefore, there were 37+44=81 *Asym* and 37 *Sym* carotids. Color Duplex Ultrasound Scanning (CDUS) using Esaote MyLab 70 modality (Milan, Italy) with a 10 MHz linear-array transducer was used to take the images of arteries.

III. METHODS

The proposed CAD system comprises of an online system (right side of Fig. 2), which predicts the class label of an incoming patient's test image. The prediction is done by using the classifiers trained by an offline learning system (left side of Fig. 2) and the grayscale feature vector extracted from the test image. The offline classification system consists of a classification phase which computes the training parameters of the classifier. In both systems, the HOS based features are obtained from the automatically segmented FWR regions, IMT and $IMTV_{poly}$. We evaluated the Support Vector Machine (SVM), Decision Tree (DT), Radial Basis Probabilistic Neural Network (RBPNN) and K-Nearest Neighbor (KNN) classifiers as the offline learning classifiers using significant features selected by *t*-test and the respective ground truth class labels (0/1 for *Asym*/*Sym*). A training set of images was used for developing the learning classifiers and a test set for evaluating the built classifiers. Ten-fold cross validation scheme was used to evaluate the performance of the classifier. The predicted class of the unknown image and its

corresponding ground truth were compared to evaluate sensitivity, specificity, and accuracy. In case of online software implementation, the system automatically extracts the wall region from an unknown image, evaluates the clinically significant features, and the optimal classifier uses the features and its training parameters to identify the unknown class.

A. Acquisition Protocol and Image Pre-Processing

The images were acquired by standardizing the following settings of the ultrasound scanner:

i. dynamic range (which corresponds to the input dynamic of the ultrasound signal before digital discretization and before conversion into grayscale) equal to 35 dB.
ii. Persistence of the frame set to medium in order to allow a frame-rate higher than 40 frames/s.
iii. Time gain compensation curve (TGC) adjustment (the TGC is a logarithmic amplifier that is used to enhance echoes originated at a higher depth. This prevents the intensities of deepest echoes to be too small when converted to grayscale. The TGC gains can be adjusted by the sonographer. We considered the TGC settings as optimal when the anterior and posterior adventita layers had same brightness).
iv. Overall gain of the grayscale set accordingly to represent the adventita layers higher contracts but avoiding the saturation of the image.
v. Linear correspondence of the ultrasound signal to the gray level (which means that the correspondence of the digitalized value of the ultrasound signal was translated into a gray level by using a linear function).
vi. Insonation with ultrasound beam orthogonal to the arterial wall

As a pre-processing step, normalization of image was performed according to a previously

published technique[18] after the pre-requisite ultrasound settings were carried out so that all the images produce comparable and reproducible features and classification results irrespective of their different acquisition conditions. As a result of pre-processing, intensities of the adventitia layer and blood will be in the range of 190-195 and 0-5, respectively due to linear scaling of intensities.

B. Far Wall Region (FWR) Segmentation

CAMES measures the IMT by using the morphological characteristics of the CCA in two steps. In Step 1, we first reduce the image to half (called down sampling process[17]), despeckle the down-sampled image, and then capture the edges of AD_F using derivative of Gaussian Kernel with known *apriori* scale, and then up-sample the evaluated AD_F profile to estimate the Region of Interest (ROI) for Step 2 (Fig. 3A-3C). This profile is used to build the ROI by extending the profile in order to create a mask that includes the entire distal wall and part of the lumen. The basic rationale behind this step is to generate a mask which covers fully the far wall region and part of the lumen. Since in this study we had images with light plaques, we had to change the ROI size of the original CAMES version, which was suitable only for arteries without plaque. The far wall region we need consists of the medial layer, intima layer and part of the lumen. The height of the ROI is about one third the lumen size. On a healthy human subject, the lumen is one cm (~ 10 mm). We take about $1/3^{rd}$ the size of the lumen (which roughly corresponds to three times the size of the far wall), which is about three mm. Since the mm to pixel conversion is approximately 16 pixels per mm, we thus get approximately 48 pixels. We took our ROI size to $\Delta_{ROI} = 50$ pixels, to include possible light plaques. Hence, compared to the original CAMES version, the ROI vertical size was changed from 30 pixels to 50 pixels. No further technical changes were made to the original version of CAMES. In Step 2, ROI is considered, and in order

to enhance the intensity edges First Order Absolute Moment (FOAM) operator is used and finally, the LI and MA borders are heuristically determined (Fig. 3D-3F). Our fully automated system was able to recognize the carotid artery with 100% accuracy in less than one second[17]. The wall region we considered is bounded at the bottom by the adventitia profile that is automatically traced (Fig. 3.C). Therefore, what we considered to be the far wall region (FWR) is the grayscale region between the traced LI and MA wall borders (Fig. 4). The LI profile is more irregular in the case of the *Sym* images, and this irregularity has been quantified using the $IMTV_{poly}$ feature. Fig. 4 shows sample carotid *Sym* and *Asym* wall images and the corresponding zoomed FWRs.

C. Grayscale and Wall Variability Feature Extraction

Studies have shown that changes in the intimal wall region are correlated with the occurrence of symptoms[10]. We have characterized these changes using non-linear entropy features based on the HOS of these images. IMT can help to determine the anatomic extent of atherosclerosis which is then used to assess cardiovascular and cerebrovascular risks[19]. Further, an increase in the IMT is one of the earlier clinical signs of an ongoing atherosclerotic process[20]. Moreover, variability in the IMT value may be associated with atherosclerosis symptomaticity[12]. The features were extracted using Matlab custom developed codes.

Higher Order Spectra (HOS)-Based Features

Higher Order Spectra is a nonlinear method[21]. Prior to HOS feature extraction, the pre-processed images were first subjected to Radon transform, which converts a two-dimensional image into a one-dimensional data at various angles. In this study, we have performed Radon transform for every 1º and then calculated the HOS features. First, we determined the bispectrum which is a complex value and is described as

$$B(f_1, f_2) = E[X(f_1)X(f_2)X^*(f_1 + f_2)] \quad (1)$$

where *X(f)* is the Fourier transform of the signal, *X** is the complex conjugate, and *E*[.] is the expectation operation. Bispectrum is evaluated in the principal domain region (Ω) and is multiplication of the three Fourier coefficients $X(f_1)$, $X(f_2)$, and $X(f_1+f_2)$. The non-redundant region is defined as a subset of the support of the function which suffices to calculate the function in the whole region. Fourier transform of real signals result in symmetry. So, the total information may be obtained from half of the component. The entire information can be obtained from the triple products terms of HOS which can be evaluated from the non-redundant region. The bispectrum phase entropy[22] was then calculated as:

$$ePRes = \sum_n p(\psi_n) log p((\psi_n)) \quad (2)$$

where,

$$p(\psi_n) = \frac{1}{L} \sum_{\Omega} l(\phi(B(f_1, f_2)) \in \psi_n) \quad (3)$$

$$\psi_n = \{\varphi \mid -\pi + 2\pi n / N \le \varphi < -\pi + 2\pi(n+1)/N\}, \quad n = 0,1,...,N-1 \quad (4)$$

where L is the number of points within the non-redundant region, ϕ is the phase angle of the bispectrum, and *l(.)* is an indicator function which gives a value of 1 when the phase angle is within the range depicted by ψ_n in equation (4).

Two bispectral entropies are defined as:

Normalized Bispectral Entropy (*e1Res*):

$$e1Res = -\sum_i p_i log(p_i) \quad (5)$$

where,

$$p_i = \frac{|B(f_1, f_2)|}{\sum_{\Omega} |B(f_1, f_2)|} \quad (6)$$

Normalized Bispectral Squared Entropy (*e2Res*):

$$e2Res = -\sum_j q_j log(q_j) \quad (7)$$

where,

$$q_j = \frac{|B(f_1,f_2)|^2}{\sum_\Omega |B(f_1,f_2)|^2} \quad (8)$$

The total number of HOS features calculated was 540 (180 x 3). The original image was fed to the Radon transform. It rotates the image about its centre in various angles and evaluates the line integrals along the parallel paths. So, in the Radon domain, the lines of the image will become points. Hence, the 2D image is converted into a 1D parallel beam projection at different angles. Then the bispectrum was evaluated for every 1 degree. The variation in the gray levels of the image can be deciphered by the entropies. Bispctrum is a complex value with real and imaginary part. Bispectrum entropy (*eRes (78º), eRes (79º))* is the spectral entropy evaluated from the real part of bispectrum [52]. Similarly, the entropy of the phase component of the bispectrum (*ePRes (64º), ePRes (65º))* estimates the variation in the phase of the image.

IMT and IMTV variability

Polyline Distance Measure (PDM)[23] was used to estimate the length between LI and MA borders, which indicates the *IMT*. PDM evaluates the length of each vertex of one boundary to the segments of the second boundary. Let us assume two boundaries B_1 and B_2. The length *d(v,s)* between a vertex $v=(x_0,y_0)$ on B_1 and a segment *s* whose endpoints, $v_1=(x_1,y_1)$, and, $v_2=(x_2,y_2)$, on B_2 can be explained as:

$$d(v,s) = \begin{cases} d_\perp & 0 \le \lambda \le 1 \\ \min\{d_1,d_2\} & \lambda < 0, \lambda > 1 \end{cases} \quad (9)$$

where d_1 and d_2 are the Euclidean distances between the vertex *v* and the endpoints of *s*; λ is

the length along the vector of the segment *s*; $d_{\perp}$ is the perpendicular length between *v* and *s*. The polyline length from vertex *v* to the contour B_2 is termed as $d(v, B_2) = \min_{s \in B_2}\{d(v,s)\}$. The length between the vertices of B_1 to the sections of B_2 is considered as the total distances from the vertices of B_1 to the smallest segment of B_2:

$$d(B_1, B_2) = \sum_{v \in B_1} d(v, B_2) \tag{10}$$

Similarly, $d(B_2,B_1)$ can be estimated by swapping the boundaries. The distance between boundaries is given by:

$$D(B_1, B_2) = \frac{d(B_1, B_2) + d(B_2, B_1)}{(\#\text{ of vertices of } B_1 + \#\text{ of vertices of } B_2)} \tag{11}$$

Where B_1 is the LI boundary, B_2 as the MA boundary, $D(B_1, B_2)$ indicates the IMT measure. We have quantified wall variability by a new feature proposed in this work called the $IMTV_{poly}$ which is calculated by evaluating the standard deviation of the IMT. The variability in the distance measurements was first computed as:

$$\sigma^2(B_1, B_2) = \sum_{v \in B_1} \left(d(v, B_2) - d(B_1, B_2)\right)^2 \tag{12}$$

$$\sigma^2(B_2, B_1) = \sum_{v \in B_2} \left(d(v, B_1) - d(B_2, B_1)\right)^2 \tag{13}$$

and the $IMTV_{poly}$ was calculated by

$$IMTV_{poly} = \sqrt{\frac{\sigma^2(B_1, B_2) + \sigma^2(B_2, B_1)}{\#\text{ vertices of } B_1 + \#\text{ vertices of } B_2}} \tag{14}$$

The main advantage of using PDM is that the measured distance is robust because it is not dependent on the number of points on each contour and the variability is unbiased.

IV. CLASSIFIERS

Different supervised classifiers use different techniques to learn the data patterns from samples

belonging to different classes in the training dataset. Since every classifier is different in its approach, no single classifier can be considered the best for a particular dataset. Hence, we have evaluated the performance of several classifiers in this study. Support Vector Machine (SVM)[24] is a commonly used supervised classifier. Given a set of training data, SVM aims to determine a separating hyperplane that separates the data belonging to the two different groups with a highest separation between the hyperplane and the data closest to the hyperplane. In order to separate the non-linear data, kernel functions are availed to map the initial data to a higher dimensional feature space where they become linearly separable[25]. SVM classifiers have a simple geometric interpretation, yield a sparse solution and are less prone to over-fitting. The Radial Basis Function (RBF) kernel and polynomial kernels of varying orders were used in this work.

In the Radial Basis Probabilistic Neural Network (RBPNN), the radial basis layer yields a distance vector by estimating the distances between the test feature vector and training feature vectors. The next competitive layer adds these contributions for each input groups and yields a output which is the vector of probabilities. The compete transfer function at the output of the second layer chooses the maximum of these probabilities to evaluate the unknown data class. In K-Nearest Neighbor (KNN) classifier, unknown data is assigned to the class that is the most common to its K nearest neighbors. In Decision Trees (DT), tree is built using the input features, and various rules are generated from the tree. The unknown class is predicted using these rules.

V. RESULTS

A. Selected Features

Our feature extraction algorithm led to 542 features for each image. Hence, we applied a feature reduction and selection strategy, in order to keep the most relevant feature for classification and in order to avoid having collinear variables. In fact, collinear variables might

decrease the power of the classifiers by forcing to unneeded over-modeling of the data[26]. Preliminary, we tested if the single features had normal distribution using the Quantile-Quantile plot (Q-Q plot) and the *Goodness-of-fit* χ^2 test and found that we could not reject the hypothesis of normal distributions. Then, we applied a one-way ANOVA to the features. We considered the pathology as independent variable and we assessed which features could be considered as statistically different between the *Sym* and *Asym* groups. We considered a feature to be statistically significant (*i.e.*, different between the two groups) if the *p* value was lower than 0.05. All variables with *p* value higher than 0.05 were not considered for classification. This feature reduction approach was already used in several multivariate and metabolomics studies[26], because the ANOVA analysis is quite robust to violation of the hypothesis of normal distribution of the variables[27]. Table I presents the seven features selected out of the 542 initially extracted features. As highlighted under Section III. C, *IMT* and $IMTV_{poly}$ features characterize the early atherosclerotic process[19,20]. Therefore, even though the *p*-value is not less than 0.05 for *IMT* and $IMTV_{poly}$, on using them in classifiers, we found that they significantly improved the accuracy. We feel that the novel combination of these features have better separated the samples belonging to the two classes, and, resulted in the highest accuracy. Two clinically significant phase entropy based features were extracted for Radon transform angles $\theta = 64^0$ and $\theta = 65^0$. (*ePRes*(64^0) and *ePRes*(65^0)). Three normalized bispectral entropies extracted at $\theta = 77^0$, $\theta = 78^0$, and $\theta = 79^0$ (*e1Res*(77^0), *e1Res*(78^0) and *e1Res*(79^0)) were also significant. In the case of $IMTV_{poly}$, the *Sym* images showed a higher variability than the *Asym* images.

B. Classification Results

To obtain more generalized and robust performance measures, ten-fold cross validation

method was used for resampling wherein the dataset is split into ten folds. In the first run, first nine folds were availed for training the classifier and the last one fold was availed for testing and evaluation of the performance measures. This procedure was repeated nine more times by taking different fold as testing data every time. The averages of those obtained in each run is considered as the overall performance of the classifier. This procedure was stratified such that the ratio of the samples belonging to the two classes remained the same in every run i.e., in each run, 34 *Sym* and 73 *Asym* images were used for training, and 3 *Sym* and 8 *Asym* images were used for testing. The average sensitivity, specificity, accuracy, and PPV values obtained by feeding all the features except the $IMTV_{poly}$ and *IMT* feature and by feeding all features including *IMT* and $IMTV_{poly}$ into the classifiers are presented in Table II. It is evident that the classifiers show improved performance when *IMT* and $IMTV_{poly}$ are included in the training process. An average sensitivity and specificity of 100% and accuracy of 99.1% was reported using SVM classifier with polynomial kernel of order 3. Thus, these two features are more sensitive in capturing the possible plaque onset information. This is because the plaque deposit usually covers the LI border, and thus, the LI border has more variability, which is captured by $IMTV_{poly}$. Moreover, we also used features extracted from manually segmented FWRs in these classifiers and obtained the same accuracy of 99.1% emphasizing the reliability of our CAMES segmentation paradigm.

SVM classifier uses two parameters (i) sigma (σ) and (ii) cost function. Sigma helps to control the degree of nonlinearity and C assists in controlling the over-fitting of the model. We have evaluated, C = 100, σ = 0.001, and number of support vectors = 9 using grid search method in order to obtain the highest classification accuracy. In the case of the fuzzy classifier, the clusters were based on each of the seven input features i.e. the input membership functions, and eight rules were obtained. In the RBPNN classifier, biases were fixed to $\sqrt{\ln 0.5}/s$, where s=spread

constant of RBPNN, which was 0.1 for maximum accuracy. In KNN classifier, we achieved the maximum accuracy for K=5.

We repeated the same classification scheme by using the IMT alone, then $IMTV_{poly}$ alone, and the combination of IMT and $IMTV_{poly}$. The SVM classifier showed an average accuracy equal to about 85%, thus evidencing how the texture features of the FWR are more efficient in capturing the information contained in the ultrasound image that the IMT and $IMTV_{poly}$ alone.

VI. DISCUSSION

Previously developed CAD systems were mainly devoted to plaque classification. Kyriacou et al.[6] reviewed many CAD algorithms that were developed to classify the detected plaques. Christodoulou et al.[7] obtained shape features and 61 textures from manually segmented ROIs of 230 plaque images, used them in a modular neural network, and presented a classification accuracy of 73.1%. Mougiakakou et al.[8] used 21 first-order statistical features and Laws' texture energy features extracted from 54 *Sym* and 54 *Asym* plaques in a novel hybrid neural network and obtained a high accuracy of 99.1%. This high accuracy was achieved only after manual segmentation of the plaque. In 2005, Kyriacou et al.[28] used morphological features and ten texture along with statistical and neural classifiers and presented 71.2% of classification accuracy. Later, they determined the normalized pattern spectra for binary and grayscale models, and used them in SVM and probabilistic neural network classifiers. The highest accuracy of 73.7% was registered by SVM on evaluating 137 cases in each class. In 2009, Seabra et al. [14] extracted Rayleigh parameters, morphological, histogram and texture features from 102 *Asym* and 44 *Sym* plaques. One hundred and fourteen significant features were derived from various images, called normalized, noiseless, envelope, and speckle images. Again, manual ROI

selection was done.

In our previous work[30,31], using combination of higher order spectra (HOS), textures and discrete wavelet transform features using Portugal database we obtained an average sensitivity of 97%, an accuracy of 91.7%, and specificity of 80%. We reported the classification accuracies of 93.1% and 85.3%, respectively.

Hence, by summarizing, the aforementioned CAD studies shoed either low accuracy or a considerable number of features to perform classification. Moreover, mostly any previous study required manual delineation of the ROI, thus introducing inter-operator variability. In this regard, our Atheromatic™ system presents relatively high classification accuracy using a small feature set extracted from automatically segmented FWR. Moreover, the novelty of our work lies in the fact that we studied the FWR by using the *IMT* and $IMTV_{poly}$ features of the distal wall instead of the plaque regions and obtained a high accuracy of 100% to differentiate *Sym* and *Asym* cases based on early changes in the FWR. The key points of our study can be summarized as follows: (1) by using a reduced feature set (seven features) we could obtain high classification performance; (2) the technique is suitable to be tested in a clinical environment, because the clinician simply has to feed the ultrasound image to get the classification (the entire process of segmentation and classification requires less than 20 minutes); (3) the high classification performance indicates that this system could be further explored as a possible adjunct diagnostic system; (4) the system is totally user independent and, thus, it doesn't introduce inter-operator variability into the classification results.

Since atherosclerotic lesions begin in the artery wall, in this work, we characterized the subtle textural changes in the automatically segmented wall region of carotid images of *Sym* and *Asym* patients using powerful non-linear HOS features, *IMT* and *IMT* wall variability. We included in

the study patients with either TIA/stroke and discarded all the patients with possible confounding factors at cerebral level (i.e. patent foramen ovale or atrial septal defect, suspected pulmonary embolism, etc…). Therefore, we assumed that the origin of the TIA/stroke was directly correlated to the ipsilateral carotid.

We demonstrated that Atheromatic™ features using SVM classifier presented a high classification accuracy of 99.1%. We make the following conclusions from our study: (a) textural changes in the far wall of carotid ultrasound images can help in accurate *Sym* vs. *Asym* classification; (b) the most commonly studied wall variability feature $IMTV_{poly}$ and *IMT* can be powerful features for far wall region classification; and (c) high accuracy can be achieved using far wall regions that were automatically segmented using our published validated automated CAMES algorithm.

Although the dataset size used in this study can be increased over time, we have demonstrated good accuracy. However, more validation is needed on large datasets collected from other institutes with different gain settings. Our future work also includes the use of significant features such as Carotid Artery Wall Thickness (CAWT) and fractal dimension, for *Sym* and *Asym* classification, and the possible extension of the technique to 3D characterization. We also intend to study this technique on plaque ROIs.

References

1. Ross R. Atherosclerosis--an inflammatory disease. N Engl J Med 1999;340.
2. Carter-Monroe N, Yazdani S, Ladich E, et al. Introduction to the Pathology of Carotid Atherosclerosis: Histologic Classification and Imaging Correlation. In: Suri JS, Kathuria C, Molinari F, editors. Atherosclerosis Disease Management: Springer New York; 2011. p 3.

3. Organization WH. Cardiovascular disease. 2012.

4. Polak JF, Shemanski L, O'Leary DH, et al. Hypoechoic plaque at US of the carotid artery: an independent risk factor for incident stroke in adults aged 65 years or older. Cardiovascular Health Study. Radiology 1998;208.

5. Inzitari D, Eliasziw M, Gates P, et al. The causes and risk of stroke in patients with asymptomatic internal-carotid-artery stenosis. North American Symptomatic Carotid Endarterectomy Trial Collaborators. N Engl J Med 2000;342.

6. Kyriacou EC, Pattichis C, Pattichis M, et al. A review of noninvasive ultrasound image processing methods in the analysis of carotid plaque morphology for the assessment of stroke risk. IEEE Trans Inf Technol Biomed 2010;14.

7. Christodoulou CI, Pattichis CS, Pantziaris M, et al. Texture-based classification of atherosclerotic carotid plaques. Medical Imaging, IEEE Transactions on 2003;22.

8. Mougiakakou SG, Golemati S, Gousias I, et al. Computer-aided diagnosis of carotid atherosclerosis based on ultrasound image statistics, laws' texture and neural networks. Ultrasound Med Biol 2007;33.

9. AbuRahma AF, Wulu JT, Jr., Crotty B. Carotid plaque ultrasonic heterogeneity and severity of stenosis. Stroke 2002;33.

10. Virmani R, Kolodgie FD, Burke AP, et al. Lessons from sudden coronary death: a comprehensive morphological classification scheme for atherosclerotic lesions. Arterioscler Thromb Vasc Biol 2000;20.

11. Cheng X, Zhou Y, Jin Y, et al. Intima-medial thickness homogeneity in the common carotid artery: measurement method and preliminary clinical study. J Clin Ultrasound 2012;40.

12. Saba L, Meiburger KM, Molinari F, et al. Carotid IMT Variability (IMTV) and Its Validation in Symptomatic versus Asymptomatic Italian Population: Can This Be a Useful Index for Studying Symptomaticity? Echocardiography 2012;29.

13. Molinari F, Zeng G, Suri JS. A state of the art review on intima-media thickness (IMT) measurement and wall segmentation techniques for carotid ultrasound. Computer Methods and Programs in Biomedicine 2010;100:201.

14. Molinari F, Zeng G, Suri J. Greedy technique and its validation for fusion of two segmentation paradigms leads to an accurate intima-media thickness measure in plaque carotid arterial ultrasound. The Journal for Vascular Ultrasound 2010;34.

15. Molinari F, Meiburger KM, Saba L, et al. Constrained snake vs. conventional snake for carotid ultrasound automated IMT measurements on multi-center data sets. Ultrasonics 2012;52.

16. Molinari F, Meiburger KM, Saba L, et al. Fully automated dual-snake formulation for carotid intima-media thickness measurement: a new approach. J Ultrasound Med 2012;31.

17. Molinari F, Pattichis CS, Zeng G, et al. Completely automated multiresolution edge snapper--a new technique for an accurate carotid ultrasound IMT measurement: clinical validation and benchmarking on a multi-institutional database. IEEE Trans Image Process 2012;21.

18. Elatrozy T, Nicolaides A, Tegos T, et al. The effect of B-mode ultrasonic image standardisation on the echodensity of symptomatic and asymptomatic carotid bifurcation plaques. Int Angiol 1998;17.

19. Lorenz MW, Markus HS, Bots ML, et al. Prediction of clinical cardiovascular events with carotid intima-media thickness: a systematic review and meta-analysis. Circulation 2007;115.

20. Touboul PJ, Hennerici MG, Meairs S, et al. Mannheim carotid intima-media thickness consensus (2004-2006). An update on behalf of the Advisory Board of the 3rd and 4th Watching the Risk Symposium, 13th and 15th European Stroke Conferences, Mannheim, Germany, 2004, and Brussels, Belgium, 2006. Cerebrovasc Dis 2007;23.

21. Nikias CL, Petropulu AP. Higher-order spectra analysis: a nonlinear signal processing framework: PTR Prentice Hall; 1993.

22. Acharya UR, Molinari F, Sree SV, et al. Automated diagnosis of epileptic EEG using entropies. Biomedical Signal Processing and Control 2012;7.

23. Saba L, Molinari F, Meiburger KM, et al. What is the correct distance measurement metric when measuring carotid ultrasound intima-media thickness automatically? International Angiology 2012,31.

24. Sánchez A VD. Advanced support vector machines and kernel methods. Neurocomputing 2003;55.

25. Muller K, Mika S, Ratsch G, et al. An introduction to kernel-based learning algorithms. Neural Networks, IEEE Transactions on 2001;12.

26. Molinari F, Rosati S, Liboni W, et al. Time-Frequency Characterization of Cerebral Hemodynamics of Migraine Sufferers as Assessed by NIRS Signals. Eurasip J Adv Sig Pr 2010.

27. Blaise BJ, Navratil V, Domange C, et al. Two-dimensional statistical recoupling for the identification of perturbed metabolic networks from NMR spectroscopy. Journal of proteome research 2010;9.

28. Kyriacou E, Pattichis MS, Christodoulou CI, et al. Ultrasound imaging in the analysis of carotid plaque morphology for the assessment of stroke. Stud Health Technol Inform 2005;113.

29. Seabra J, Pedro LM, Fernandes EFJ, et al. Ultrasonographic characterization and identification of symptomatic carotid plaques. Conf Proc IEEE Eng Med Biol Soc 2010;2010.

30. Acharya UR, Faust O, Sree VS, et al. Understanding symptomatology of atherosclerotic plaque by image-based tissue characterization. Comput Methods Programs Biomed 2013;110.

31. Acharya UR, Mookiah MR, Vinitha Sree S, et al. Atherosclerotic plaque tissue characterization in 2D ultrasound longitudinal carotid scans for automated classification: a paradigm for stroke risk assessment. Med Biol Eng Comput 2013;51.

Figure Legends

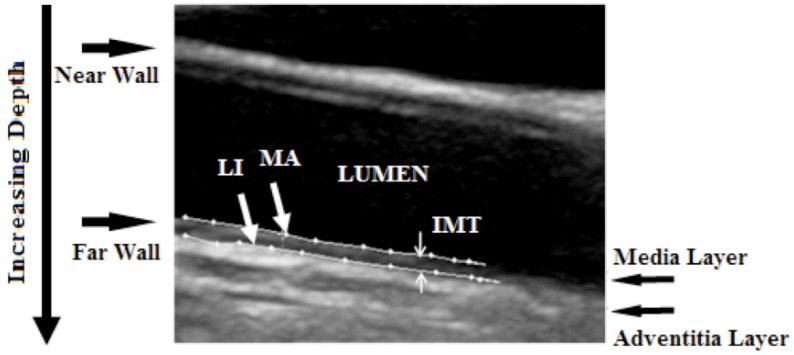

Fig. 1 Echographic appearance of a CCA in longitudinal projection

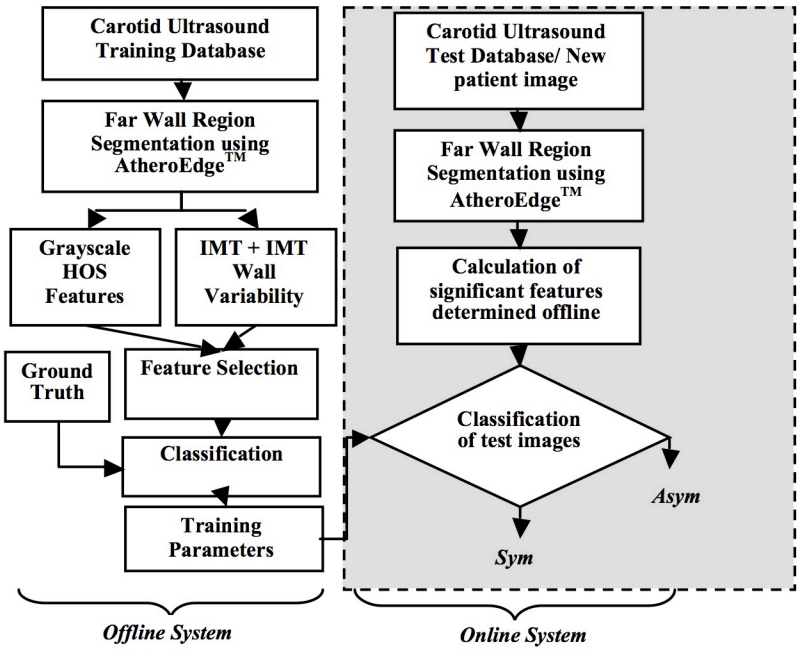

Fig. 2. The proposed system.

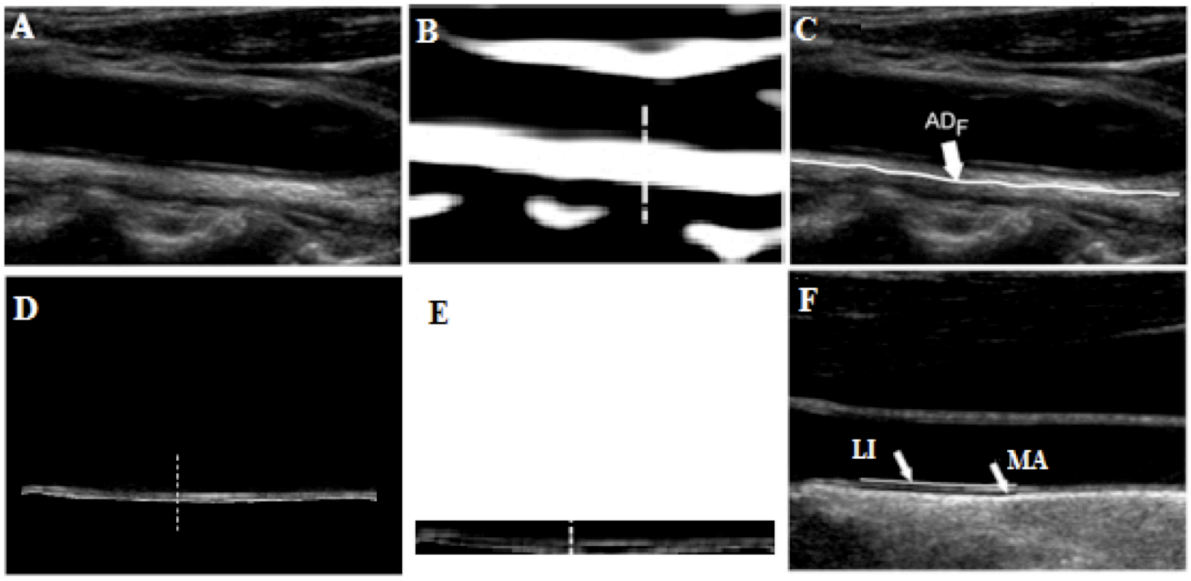

Fig. 3. (A) Original B-mode image. (B) Downsampled and despeckled image with recognized near and far adventitia profiles (C) Traced AD_F profile (D) The region of interest around the automatically traced AD_F (E) FOAM operator (F) Final LI and MA tracings.

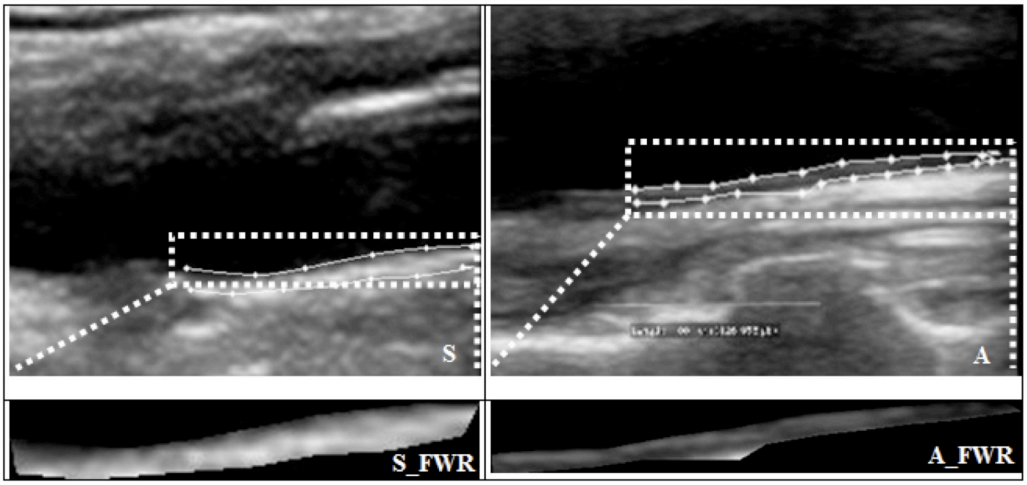

Fig. 4. (S) and (A) show sample *Sym* and *Asym* wall images. They show the traced LI and MA wall borders (S_FWR) and (A_FWR) show the corresponding zoomed wall Far Wall Regions (FWR).

TABLE I

RANGE (MEAN ± STANDARD DEVIATION) OF THE SELECTED FEATURES

Feature	***Asym***	***Sym***	***p*-value**
e1Res (77º)	0.327±0.075	0.299±0.059	0.023
e1Res (78º)	0.329±0.074	0.299±0.056	0.019
e1Res (79º)	0.330±0.074	0.299±0.052	0.018
ePRes (64º)	3.568±0.010	3.557±0.028	0.044
ePRes (65º)	3.566±0.014	3.559±0.024	0.040
IMT	1.001±0.324	1.134±1.507	0.102
$IMTV_{poly}$	0.155±0.118	0.172±0.204	0.902

TABLE II

PERFORMANCE OF THE ATHEROMATIC SYSTEM

(A: ACCURACY; SN: SENSITIVITY; SP: SPECIFICITY) (ALL VALUES IN %)

	All features of Table I except $IMTV_{poly}$ and IMT				All features including Table I			
Classifier	A	PPV	Sn	Sp	A	PPV	Sn	Sp
SVM								
Linear	91.8	89.2	83.3	95	97.3	97.5	93.3	98.8
Poly Order 1	90	85	80	93.8	97.3	97.5	93.3	98.8
Poly Order 2	90	85	80	93.8	98.2	97.5	96.7	98.8
Poly Order 3	90	87.5	76.7	95	99.1	100	96.7	100
RBF	89.1	83.3	76.7	93.8	99.1	100	96.7	100
Other classifiers								
KNN	88.2	80.8	80	91.3	92.7	93.3	80	97.5
RBPNN	5	82.7	67.5	60	89.1	96.7	63.3	98.8
DT	5	80	67.6	66.7	89.1	89.3	73.3	95